Journal of Solid State Chemistry 339 (2024) 124920

Contents lists available at ScienceDirect

Journal of Solid State Chemistry

journal homepage: www.elsevier.com/locate/yjssc

Second-harmonic generation effect enhanced by Li substitution for Na in $Li_1(Li_XNa_{5-X})Mo_9O_{30}$

V.Z. Vuksan [a], Y. Cheng [a], S.-H. Park [a,*], E.V. Sturm [a], K. Gméling [b], L. Szentmiklósi [b]

[a] Section Crystallography, Dept. Earth & Environmental Sciences, Ludwig-Maximilians-Universität München, Munich, 80333, Germany
[b] HUN-REN, Centre for Energy Research, Hungarian Academy of Sciences, Budapest, 1121, Hungary

ARTICLE INFO

MSC:
81-08
42B05

Keywords:
Second-harmonic generation
Li-Na-molybdates
Structure-related optical properties

ABSTRACT

Large single crystals of the solid-solution series $Li_1(Li_XNa_{5-X})Mo_9O_{30}$ were grown by the Czochralski method by varying the Li substitution for Na. Structure analyses with X-ray single-crystal diffraction data elucidated statistic disorder of Li with Na at three independent Na sites. The resulting Li substitution X = 0, 1.2, and 2.8 could be confirmed by neutron activation analysis. Second-harmonic generation (SHG) light intensities and non-linear optical (NLO) coefficients were determined in three crystallographic main directions by Maker fringe measurements. DFT calculations delivered absolute NLO magnitudes. UV/Vis optical spectra revealed that the transmission rises from X = 0 to X = 2.8. However, the SHG effect is at largest in $Li_1(Li_{1.2}Na_{3.8})Mo_9O_{30}$ (X = 1.2), so far investigated in this study.

1. Introduction

Critical crystal properties for effective second-harmonic generation (SHG), i.e., frequency-doubling are associated with high non-linear optical (NLO) parameters, low refractive indices [1], and high transmission of the generated SHG light at a high laser damage threshold [2–4]. From a structural point of view, the absence of space inversion is the important condition for realizing SHG with the non-zero second-order electric polarization P in the crystal of interest: $P = \epsilon_0 E^2 \chi^{(2)} \neq 0$ (ϵ_0: vacuum permittivity; E: external electric Field; $\chi^{(2)}$: the second-order electric susceptibility). For centrosymmetric media, $P = -P$ is valid only for $\chi^{(2)} = 0$. This applies to all even-ordered non-linear polarization in a non-centrosymmetric crystal.

Several molybdates have been studied for non-linear optical processes [5]. Nanoparticles of Ag_2MoO_4 were investigated for the use as nanoseconds-lasers and optical limiters with a high optical limiting threshold at 10^{12} W/m^2. These SHG applications are realized by varying nanoparticle size to control the ranges both of band gap and absorption [6]. Single crystals of $ZnMoO_4$ [7], Li_2MoO_4 [8], and $CaMoO_4$ with promising optical and luminescent properties are suited as scintillating materials for ^{100}Mo-based bolometers [9]. Particularly, $CaMoO_4$ shows high mechanical and thermal stability. Its high thermal conductivity and optimal refractive index stands up as a solid state Raman-active material as well as an interesting SHG media in optoelectronics [10]. To investigate direction-dependent SHG effects it is necessary to grow several cm-sized, high-quality crystals. Zhang et al. [11] were successful in growing large single crystals of $Li_1Na_5Mo_9O_{30}$ using the Czochralski and Kyropolous methods, allowing Maker fringe measurements [12] to determine its NLO parameters of d_{31} = 1.4 pm/V, d_{32} = 4.3 pm/V and d_{33} = 1.1 pm/V. In addition, results from UV/Vis spectroscopy and laser damage threshold experiments could deliver its suitability as a medium for SHG lasers; its wide transmission range for electromagnetic radiation is from 357 nm to 5.26 μm at high laser damage threshold of 1.2 GW/cm^2 [11]. On the other hand, the Czochralski growth process could be modeled for optimal growing conditions of $Li_1Na_5Mo_9O_{30}$ to improve laser damage threshold of 15–16 GW/cm^2 [13] for luminescence under UV-excitation. Based on these previous investigations, our interest in $Li_1Na_5Mo_9O_{30}$ arises from further factors relevant to study direction-dependent SHG effects: Na at three unique sites can be partially substituted by Li to increase the polarizability and the transmission over the UV/Vis range, and hence the SHG effect is enhanced possibly in the resulting solid-solution crystals. In addition, large single crystal growth of $Li_1Na_5Mo_9O_{30}$ is relatively simple at ca. 500 ° C in air.

The crystal structure of $Li_1Na_5Mo_9O_{30}$ (Fig. 1(a)) in a polar and non-centrosymmetric space group symmetry, $Fdd2$ [14] is built with edge- and vertex-sharing clusters of MoO_6 octahedra (Fig. 1(b)). Five independent Mo sites (Mo1-Mo5) make each 9er-MoO_6 cluster (Fig. 2(a)) which are connected to each other by LiO_6 and NaO_6 moieties. There is one unique Li site making pure LiO_6 octahedra while three independent

* Corresponding author.
E-mail addresses: victor.vuksan@campus.lmu.de (V.Z. Vuksan), Yaoshi.Cheng@campus.lmu.de (Y. Cheng), sohyun.park@lmu.de (S.-H. Park), sturm.elena@lmu.de (E.V. Sturm), naa@bnc.hu (K. Gméling), szentmiklosi.laszlo@ek-cer.hu (L. Szentmiklósi).

https://doi.org/10.1016/j.jssc.2024.124920
Received 10 May 2024; Received in revised form 10 July 2024; Accepted 24 July 2024
Available online 26 July 2024

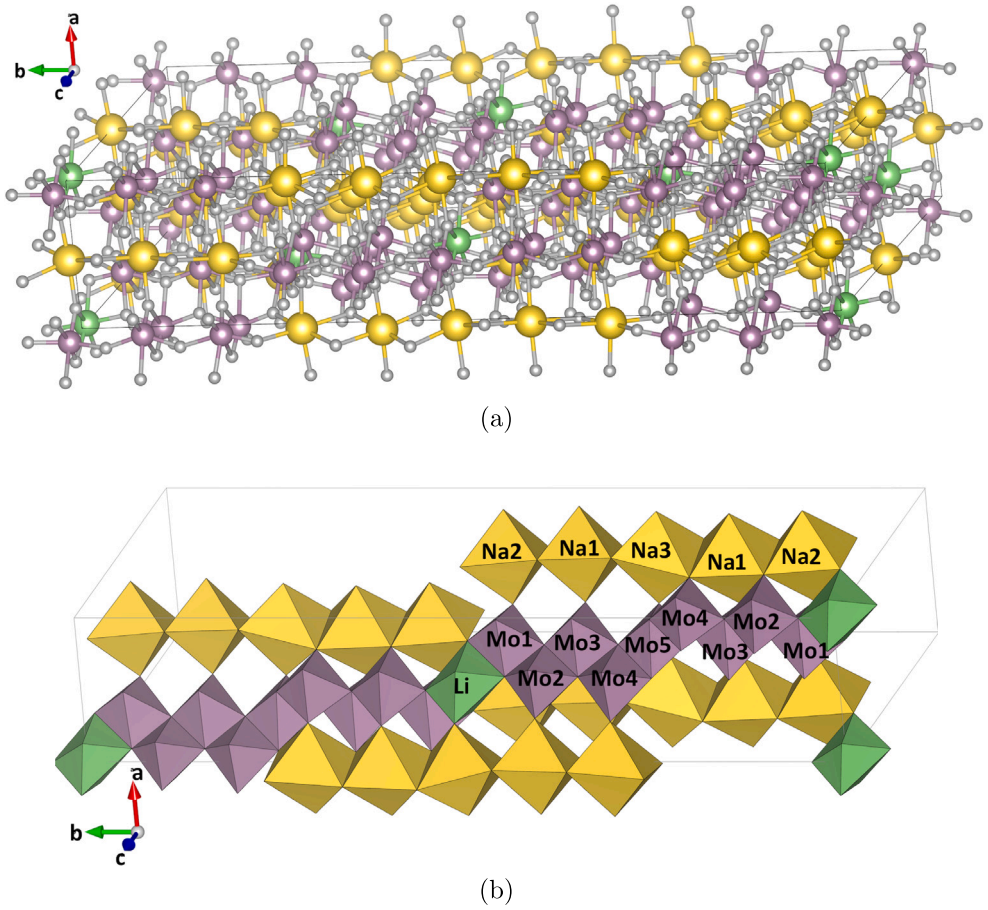

Fig. 1. (a) The arrangement of Na (yellow), Mo (purple), Li (green) and O (light gray) atoms with interatomic bonds (bars) within a unit cell of $Li_1Na_5Mo_9O_{30}$. (b) Structural building units of $Li_1Na_5Mo_9O_{30}$ in which 9er-MoO_6 cluster (purple) is connected to each other by slabs of NaO_6 (yellow) with single LiO_6 (light green). The unit cell is framed in gray.

Na sites (Na1, Na2, and Na3) form a 5er-slab of $Na2O_6$-$Na1O_6$-$Na3O_6$-$Na1O_6$-$Na2O_6$ (Fig. 2(b)). The NaO_6 slabs are configured parallel to the crystallographic ***b*** axis, where Li can occupy Na sites to build a solid-solution series $Li_1(Li_XNa_{5-X})Mo_9O_{30}$. This report presents crystal growth of three new $Li_1(Li_XNa_{5-X})Mo_9O_{30}$ solid-solution compounds. Their direction-dependent NLO parameters and SHG light intensities were experimentally and theoretically determined and discussed in the context of Li amounts in NaO_6 slabs.

2. Materials and methods

2.1. Crystal growth and preparation for direction-dependent optical characterization

Three different single crystals of $Li_1(Li_XNa_{5-X})Mo_9O_{30}$ were grown using the Czochralski method in the present study, referring to previous works [11,13] on crystal growth of $Li_1Na_5Mo_9O_{30}$. A part of crystals of $Li_1Na_5Mo_9O_{30}$ from preliminary experiments were oriented-cut in the length direction parallel to [001] and used as seeds. Each seed crystal was fixed with platinum wire to the corundum pulling rod. All crystal growth experiments were conducted under ambient atmosphere using a home-constructed high-temperature growth apparatus [15]. Li/Na molar ratios, growth temperatures and pulling rates were varied. The growth temperatures selected were in accordance to the melting points descending with increasing the Li/Na ratio in this system, based on differential thermal analysis in our previous study [Buyan Arivjikh et al. to be published elsewhere]. Details of crystal growth parameters of the three samples denoted as Sample#n (n = 1–3) are given in Table 1.

For direction-dependent optical measurements, the obtained three crystal samples were oriented parallel to (100), (010) and (001) planes on a Laue camera using a molybdenum X-ray tube. The oriented crystals were cut to plates before polishing to perform Maker fringe measurements.

2.2. X-ray single crystal diffraction (XSD)

XSD was conducted with small single crystal pieces of Sample#1, -#2, and -#3. Each single crystal was attached with two-component adhesive to a thin glass fiber within a brass sample holder and mounted onto a goniometer. The full reciprocal sphere was scanned with a 2D charge-coupled detector (CCD, *Atlas*) on a four-circle *Kappa* single crystal diffractometer (*Gemini-A Ultra*, Rigaku-Oxford Diffraction) using Mo$K_{\alpha1}$ (0.7093 Å, graphite(002) monochromator) at room temperature (RT). The exposure time was varied with the resolution region up to d = 0.6 Å at a crystal-detector distance of 55 mm at $\Delta(\phi) = 1°$ step size. Data reduction including numerical absorption correction [16] was executed with the software CrysAlisPro (Rigaku-Oxford Diffraction) [17] for each XSD data set with high average redundancy of 17–18 at d = 0.6 Å. Experimental parameters of the XSD are listed in Table 2.

2.3. Structure analysis

Structure solution was executed with XSD data of Sample#1 using the option Direct Method embedded in the program package SHELX [18]. The obtained starting model was used for further XSD data analyses by least-squares against squared structure factors (F^2) with the option Difference Fourier in the program suite Jana2020 [19].

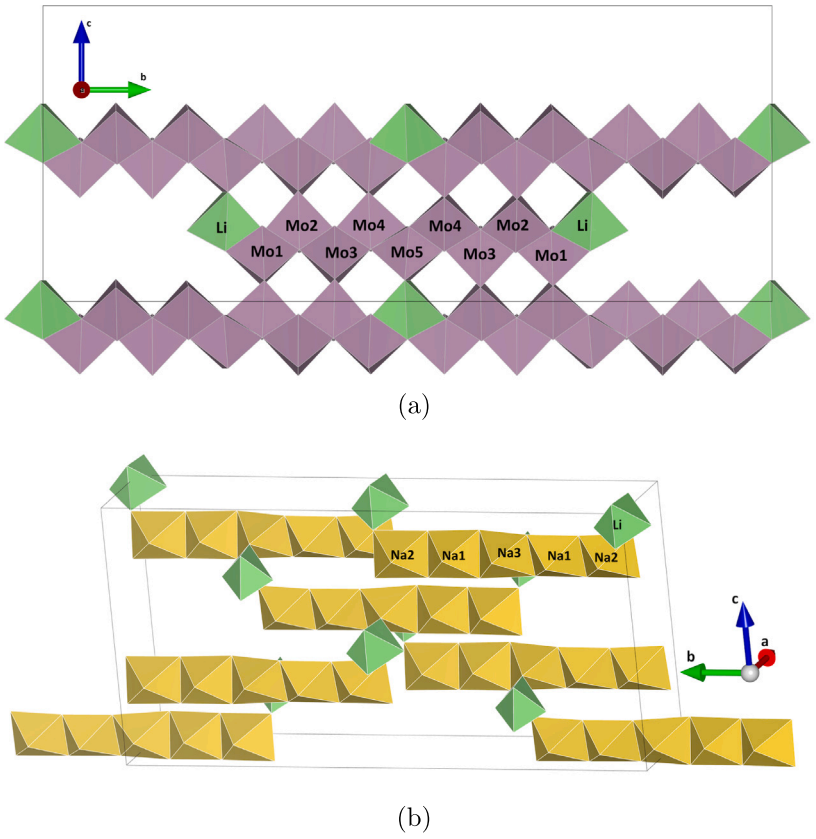

Fig. 2. (a) Arrangement of a 9er edge- and corner-connected MoO_6 cluster at five different Mo sites. LiO_6 centered at Li site shares one corner and two edges with MoO_6 clusters. (b) Arrangement of NaO_6 slabs. Each NaO_6 slab consists of five edge-connected NaO_6 octahedra along the ***b*** axis. LiO_6 connects two 5er NaO_6 slabs over two common corners. This part structure is the basis for the title solid-solution system.

Table 1
Crystal growth parameters in the Czochralski method applied to three different compounds of $Li_1(Li_XNa_{5-X})Mo_9O_{30}$. Samples#2 and -#3 were grown from the same starting mixture composition but at different growth temperatures and pulling rates.

Sample	Growth temperature [° C]	Pulling rate [mm/h]	Li:Na molar ratio in educt
#1	540.4(1)	0.5(1)	1:5
#2	528.4(1)	1.1(1)	3:3
#3	524.4(1)	0.7(1)	3:3

Table 2
Experimental parameters of XSD data ($MoK_{\alpha 1}$) of Sample #1-#3. The quality of each data set is given by the internal agreement factor R_{int} while those of the refined structure models in the space group symmetry *Fdd*2 are expressed by the residual values R and wR^2. Their mathematical definitions are given at the bottom.

Sample		#1	#2	#3
a [Å]		7.2338(2)	7.1458(1)	6.9627(2)
b [Å]		37.1412(6)	37.1420(3)	37.1609(5)
c [Å]		17.9551(2)	17.9141(1)	17.8885(3)
V [Å^3]		4824.0(2)	4754.6(1)	4628.5(1)
Density [g/cm^3]		4.035(1)	4.004(1)	4.111(1)
Data range	h	−12~12	−11~12	−11~11
	k	−62~63	−60~60	−62~61
	l	−30~30	−30~30	−29 ~30
Total reflections		57 742	56 485	53 877
Unique reflections		6298	6207	5900
Redundancy		18.2	18.1	17.9
Absorption correction	T_{min}	0.48(1)	0.62(1)	0.42(1)
	T_{max}	1.00	1.00	1.00
Linear absorption coefficient	μ [1/cm]	4.736	4.767	4.897
[a]R_{int}		0.036	0.032	0.044
R(all, against F)		2.25	2.01	3.18
[b]wR^2(all, against I)		5.78	5.51	7.62

[a] $R_{int} = \frac{\sum_i^n |F^2_{i(obs)} - \langle F^2_{i(obs)} \rangle|}{\sum_i^n F^2_{i(obs)}}$.

[b] $wR^2 = ((\sum_i w_i (y_{calc,i} - y_{obs,i})^2)/(\sum_i w_i (y_{obs,i})^2))^{1/2}$; $w_i = 1/\sigma_i^2$.

For the structure refinement of Sample#1, all occupancy (OCC) parameters were fixed to be fully occupied, corresponding to the ideal endmember $Li_1Na_5Mo_9O_{30}$ [14]. This is particularly to compare OCC values at three independent Na sites in the models for Sample#2 and -#3 synthesized with higher amounts of Li than Sample#1 (Table 1). All atomic parameters of Sample#1, including anisotropic atomic displacement parameters (ADPs) could be refined simultaneously without high correlations (<0.9). Using this as a starting model, all atomic parameters were refined with XSD data of Sample#2 and -#3 while fixing the ADPs at three Na sites to those values for the respective ADPs refined for the structure of Sample#1. Except for these constraints, all atomic parameters were simultaneously refined without high correlations between them. The agreement factors of the three refined structures are given in Table 2. The obtained structure models were illustrated using the software VESTA [20]. The Best Fitted Idealized Polyhedra (BFIP) method [21] was used to calculate polyhedral distortion in the refined three structure models. The dipole moment of each polyhedron was calculated based on the bond-valence sum [22].

2.4. Neutron activation analysis (NAA)

Neutron-induced radioisotopes ^{24}Na and ^{99}Mo, formed during irradiation in a research reactor, are applicable to quantify the Na/Mo ratio in a non-destructive way. NAA was conducted to determine Na/Mo ratios in Sample#1 and -#2 at the NAA laboratory of the Budapest Neutron Center (BNC). The samples were activated with neutrons for 15 min that had a thermal to epithermal flux ratio of 38.0(2). A dose rate of gamma radiation of 100 μS/h was measured at a distance of 15 cm from the sample. In a spectral range of 50–3300 keV, all isotope nuclei were detected on the D5 gamma spectrometer (*Ortec 55% HPGe detector; ORTEC DSPEC 502 digital spectrometer*). Epithermal self-shielding correction was applied due to the high absorption rate of neutrons by Mo [23].

2.5. UV/Vis spectroscopy

Transmission spectroscopy in the ultra-violet and visual light range (UV/Vis) was performed to investigate the influence of Li substitution on the transmission of the prepared solid-solution series. All oriented-cut plates of three single crystal samples (Table 1) were probed on a UV/Vis transmission spectrometer (*Cary 60 UV/Vis*, Agilent). Each oriented single crystal plate was positioned into a solid-sample holder and illuminated by a Xe-discharge lamp. A spectral range of 190–1100 nm was recorded at a scan speed of 60 nm/min using the software suite *UV*Win and normalized by the sample thickness.

2.6. DFT calculations

Based on the electron density and exchange–correlation approximations, it is possible to get the behaviors of electrons and atomic nuclei of researching system by solving Kohn–Sham equation, so called as density functional theory (DFT) [24]. As a reliable first-principles calculation method, it has been widely used for predicting the physical and chemical properties of solid materials, such as elastic properties [25], optical properties [26] or vibrational properties [27]. In this work, the calculations of non-linear optical properties have been performed using the CASTEP (Cambridge Serial Total Energy Package) software [28] with the On-the-fly pseudopotential generation (OTFG) norm-conserving pseudopotentials [29]. The exchange–correlation functional were approximated by the generalized gradient approximation (GGA) with the Perdew–Burke–Ernzerhof functional [30]. Based on the structure models refined with XSD data, DFT calculations were performed to deliver direction-dependent NLO coefficients expected for three selected compounds of the title solid-solution. Unfortunately, it is not allowed setting fractional atomic occupations in the unit cell, unless building a representative supercell in which each atomic site must be fully occupied by one atom type. For this reason, DFT calculations were performed with three idealized compounds: $Li_1Na_5Mo_9O_{30}$, $Li_2Na_4Mo_9O_{30}$, and $Li_4Na_2Mo_9O_{30}$. These correspond nearly to the respective chemical composition of Sample#1, -#2, and #3 (see Results and discussion). The Monkhorst–Pack scheme k-points grid sampling was set at Γ point in the Brillouin zone. The plane-wave basis set energy cutoff was set at 625 eV. The total energy tolerance threshold was set as 2×10^{-6} eV/atom.

2.7. Optical characterization

For direction-dependent optical characterization, the large single crystals oriented-cut parallel to three crystallographic main directions were positioned to rotate around one of ***a***, ***b***, and ***c*** axes. The denotation ‖rotation axis was combined with the Li substitution amount ‘X’ to name each orientation- and composition-specific measurement. For an example, X=2.8b‖c corresponds to SHG data of the solid-solution crystal with X = 2.8 probed perpendicular to the plane (010) plate while rotating around the ***c*** axis.

In this study, non-linear optical (NLO) coefficients d_{ij} were determined by means of the rotational Maker fringe technique (MF) [12, 31] with a Ti:sapphire pulsed laser (*MIRA 900*, frep=75.6 MHz, τ_{pulse} ≈100 fs; pumped by a *Verdi V12 laser at 532 nm*, Coherent). The rotation axis of the plate sample corresponds to the polarization direction of the incoming fundamental laser beam. The samples were illuminated with a fundamental wavelength between 910 and 920 nm, filtered with a 550 nm short-pass filter. The SHG (here in 455–460 nm) beam intensity and wavelength were detected using a fiber cable (*M91L01*, Thorlabs). On the one side the fiber was attached to a collimator. On the other side it was attached to a compact Spectrometer (*CCS100*, Thorlabs). The SHG beam was measured in this way for every 0.5° incident angle in the rotating range of ±40°. To compensate for power fluctuations of the fundamental beam, the intensity at the SHG wavelength ±6.5 nm was normalized by the incoming power, which was measured by directing a small part of the fundamental beam towards a photodiode power sensor (*S120C*, Thorlabs) with a beamsplitter cube. The SHG intensity integrated at each rotating step was used to evaluate the direction-dependent NLO coefficient d_{ij} with the refractive indices n_i.

To determine frequency-dependent refractive indices n_i Brewster’s angle was measured [32] for four wavelengths, i.e., λ = 650, 512, 450, and 405 nm. The Sellmeier coefficients A, B, C, D were calculated according to $n_i^2 = A + B/(\lambda^2 - C) - D\lambda^2$ by least-squares fitting with the measured n_i values [33].

3. Results and discussion

3.1. Single crystals as-grown

Fig. 3 shows three crystals (denoted by Sample#1, -#2, and -#3), as-grown about 5.5 cm long parallel to the axis ***c***. These commonly have well-developed {010} facets. Sample#1 shows a characteristic coloring in greenish-yellow. Both other crystals tend to be pale yellowish towards colorless, and in particular Sample#3 is mostly transparent. The notably different coloring between Sample#1 and Sample#3 is mainly associated with the much higher Li/Na ratio in Sample#3, as given in Table 1. On the other hand, Sample#2 was grown at a cooling rate of 1.1(1) mm/h while Sample#3 was grown slower at 0.7(1) mm/h. This insignificantly slower crystal growth setup possibly impacts the increase of the transparency in Sample#3 although their starting mixture compositions were identical. These visual features of our crystal samples indicate that the substitution of Li for Na vary structural and optical properties in this solid-solution system. This is comprehended by results from structure analyses and optical measurements, as described in the followings.

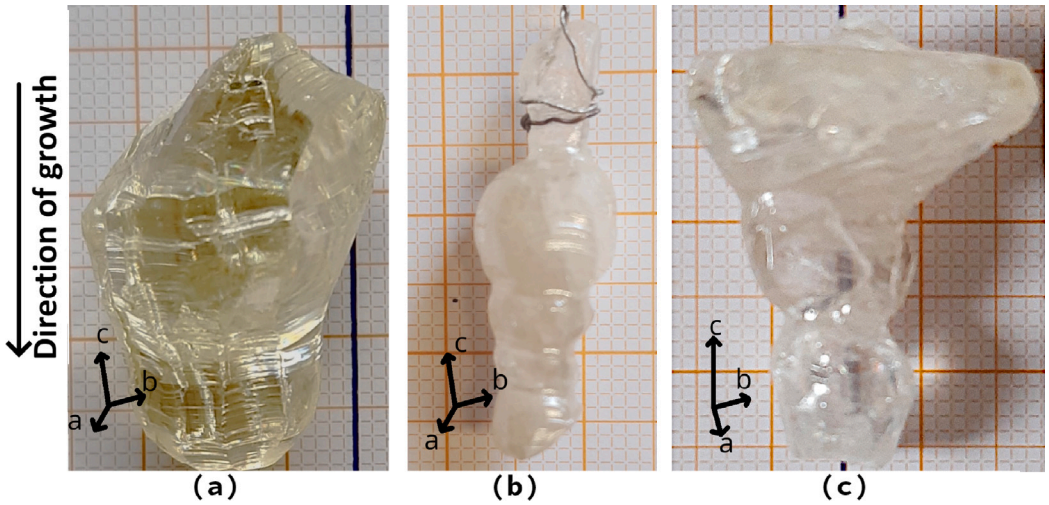

Fig. 3. Three crystal samples produced in this study. Sample#1 (a) was grown with a Li/Na ratio of 1:5, resulting in greenish-yellow coloring. Sample#2 (b) and Sample#3 (c) grown with a high Li/Na ratio of 3:3 shine pale yellowish towards colorless.

Table 3
Atomic coordinates refined with XSD data of Sample#2 (X = 1.2: $Li_1(Li_{1.2}Na_{3.8})Mo_9O_{30}$) with multiplicities (M), occupancies (OCC), and isotropic ADPs (U_{iso}). Anisotropic ADPs (U_{ij}) are given in the supplementary material (Supplementary Table A.3).

Site	Type	x	y	z	M	U_{iso}	OCC
Na1	Na	0.7658(2)	0.84793(4)	0.8006(1)	16	0.018	0.767(4)
Na2	Na	0.7445(2)	0.9533(3)	0.80281(8)	16	0.018	0.864(4)
Na3	Na	0	0	0.5481(1)	8	0.018	0.384(2)
Li	Li	0	0	0.9546(4)	8	0.023(1)	0.5
Mo1	Mo	−0.70140(3)	−0.046069(5)	0.89440(1)	16	0.01092(4)	1
Mo2	Mo	−0.78895(3)	−0.150376(4)	0.70616(1)	16	0.01022(4)	1
Mo3	Mo	−0.4469(3)	−0.100626(4)	0.64422(1)	16	0.01037(4)	1
Mo4	Mo	−0.78724(3)	−0.048287(5)	0.71592(2)	16	0.01051(4)	1
Mo5	Mo	−0.5	0	0.62008(2)	8	0.01169(5)	0.5
O1	O	−0.7069(3)	−0.00218(2)	0.7121(1)	16	0.0142(4)	1
O2	O	−0.9520(3)	−0.14819(6)	0.6370(2)	16	0.0195(6)	1
O3	O	−0.2821(3)	−0.10053(6)	0.7149(8)	16	0.0203(5)	1
O4	O	−0.7786(3)	−0.10164(4)	0.8962(1)	16	0.0133(4)	1
O5	O	−0.5410(3)	−0.05063(6)	0.9658(8)	16	0.0203(5)	1
O6	O	−0.9539(2)	−0.05279(5)	0.9505(1)	16	0.0130(4)	1
O7	O	−0.7557(3)	−0.00034(6)	0.8922(1)	16	0.0177(4)	1
O8	O	−0.9344(3)	−0.05043(6)	0.7933(1)	16	0.0178(5)	1
O9	O	−0.9175(3)	−0.15023(5)	0.7893(1)	16	0.0176(4)	1
O10	O	−0.9353(3)	−0.05066(5)	0.6402(2)	16	0.0186(5)	1
O11	O	−0.5246(3)	−0.05076(4)	0.6480(1)	16	0.0139(4)	1
O12	O	−0.7007(3)	−0.10018(4)	0.7049(1)	16	0.0124(4)	1
O13	O	−0.5544(3)	−0.15025(5)	0.8136(1)	16	0.0180(5)	1
O14	O	−0.5734(3)	−0.05361(5)	0.8104(1)	16	0.0148(4)	1
O15	O	−0.6827(3)	0.00352(6)	0.5596(1)	16	0.02110(5)	1

3.2. Structures of new solid-solution compounds varying Li/Na ratios from XSD data analyses

Results from structure solution and refinement with XSD data of Sample#1 agree with the model space group symmetry ***Fdd*2**, reported by Zhang et al. [11]. As aforementioned, OCC parameters at all atomic sites were fixed to be fully occupied for the endmember $Li_1(Na_5)Mo_9O_{30}$. Its greenish-yellow color indicates certain types of defects like color centers. However, not only for possible correlation between OCC and ADP particularly at sites of light atoms such as Li and Na, but also for results from NAA, the model was refined with OCC = 1 for all atomic sites in the endmember structure (X = 0). This refined model is given in the supplementary (Supplementary Tab.A.1).

The structure models refined with XSD data of Sample#2 and -#3 confirmed that the space group symmetry ***Fdd*2** is valid for the title solid-solution compounds. The ADPs at Na sites in the models of Sample#2 and -#3 were fixed to the respective ADP values of X = 0 to compare their OCC parameters to be refined. The unique three Na sites were refined as if Na was the only scatterer. The other atomic parameters at Li, Mo, and O sites were refined simultaneously including anisotropic ADPs with full occupation. The refined atomic parameters are listed in Tables 3 and 4.

The resulting OCC values at Na sites are far below 100% for statistic disorder of Na and Li (Tables 3 and 4). Under the assumption that all three Na sites are fully occupied by Na or Li, which could be confirmed by results from NAA, the amount of Li at each Na site was calculated with respect to the scattering power ratio of Li/Na. As a result, the respective atomic ratio of Li:Na of 9.7:30.3 and 21.9:18.1 could be obtained over all three Na sites for Samples#2 and -#3. This allows the Li substitution amount in the accumulative formula $Li_1(Li_XNa_{1-X})Mo_9O_{30}$ with X = 0, 1.2, and 2.8 in Sample#1, -#2, and -#3, respectively. From this point onward, these solid-solution compounds are denoted by X determined by XSD.

It is advantageous to use XSD as allowing the site-specific Li substitution at different Na sites. As given in Table 5, Li atoms occupy three unique Na sites in the preference Na1 > Na2 > Na3 commonly for both X = 1.2 and 2.8. This obvious tendency of Li to be found within $Na1O_6$ can be understood by its lowest octahedral distortion.

Table 4
Atomic coordinates refined with XSD-data of Sample#3 (X = 2.8: $Li_1(Li_{2.8}Na_{2.2})Mo_9O_{30}$) with multiplicities (M), occupancies (OCC), and isotropic ADPs (U_{iso}). Anisotropic ADPs are given in the supplementary material (Supplementary Table A.4).

Site	Type	x	y	z	M	U_{iso}	OCC
Na1	Na	0.7651(4)	0.84781(8)	0.8005(2)	16	0.0185	0.512(5)
Na2	Na	0.7443(4)	0.95373(6)	0.8030(2)	16	0.0185	0.603(5)
Na3	Na	0	0	0.5480(2)	8	0.0185	0.273(3)
Li	Li	0	0	0.9552(7)	8	0.0266(3)	0.5
Mo1	Mo	−0.69758(4)	−0.46016(7)	0.89446(2)	16	0.01495(6)	1
Mo2	Mo	−0.79235(5)	−0.150459(7)	0.70635(2)	16	0.01476(7)	1
Mo3	Mo	−0.43605(5)	−0.100652(6)	0.64433(2)	16	0.01562(7)	1
Mo4	Mo	−0.79121(5)	−0.04849(7)	0.71579(2)	16	0.01616(7)	1
Mo5	Mo	−0.5	0	0.62086(3)	8	0.0195(1)	0.5
O1	O	−0.7104(4)	−0.00221(7)	0.7120(2)	16	0.0181(7)	1
O2	O	−0.9602(5)	−0.14820(9)	0.6370(2)	16	0.230(9)	1
O3	O	−0.2759(6)	−0.1006(9)	0.7145(3)	16	0.262(9)	1
O4	O	−0.7763(4)	−0.10160(7)	0.8956(2)	16	0.0184(7)	1
O5	O	−0.5359(5)	−0.05011(8)	0.9662(2)	16	0.0223(7)	1
O6	O	−0.9558(4)	−0.05260(6)	0.9510(2)	16	0.0156(1)	1
O7	O	−0.7544(5)	−0.0004(8)	0.8903(2)	16	0.0187(6)	1
O8	O	−0.9397(7)	−0.0506(9)	0.7938(2)	16	0.028(1)	1
O9	O	−0.920(6)	−0.15034(8)	0.7893(2)	16	0.0243(9)	1
O10	O	−0.9430(5)	−0.05107(8)	0.6395(2)	16	0.0224(8)	1
O11	O	−0.5237(5)	−0.05068(7)	0.6473(2)	16	0.0195(7)	1
O12	O	−0.7016(4)	−0.10031(6)	0.7055(2)	16	0.0169(7)	1
O13	O	−0.5469(6)	−0.15034(8)	0.8132(2)	16	0.0244(9)	1
O14	O	−0.5677(6)	−0.05358(8)	0.8100(2)	16	0.0242(9)	1
O15	O	−0.6885(6)	0.0031(1)	0.5595(2)	16	0.0311(9)	1

	X=0	X=1.2	X=2.8
Li [%]	1.83	1.83	1.52
Na1 [%]	0.35	0.34	0.35
Na2 [%]	0.52	0.46	0.58
Na3 [%]	1.32	1.22	1.08
Mo1 [%]	2.45	2.53	2.48
Mo2 [%]	2.87	2.92	2.82
Mo3 [%]	2.52	2.56	2.56
Mo4 [%]	2.37	2.51	2.59
Mo5 [%]	1.35	1.17	1.38

(a)

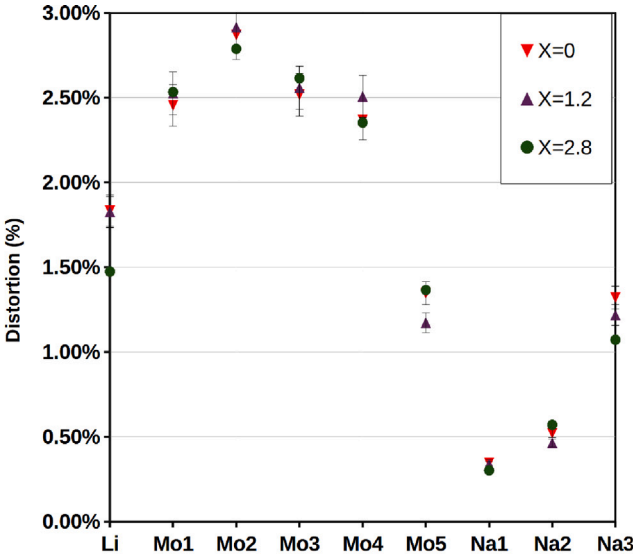

(b)

Fig. 4. (a) Octahedral distortion with respect to a perfect octahedron in [%] against X. (b) No systematic change of octahedral distortion as a function of X.

Table 5
The amount of Li and Na at three independent Na sites for X = 1.2 ($Li_1(Li_{1.2}Na_{2.8})Mo_9O_{30}$) and X = 2.8 ($Li_1(Li_{2.8}Na_{2.2})Mo_9O_{30}$), determined by XSD data analyses. The highest Li substitution occurs at Na1 site.

Li substitution	Site	Amount/site		Proportion at site [%]
		Li	Na	Li: Na
X = 1.2	Na1	5.1	10.9	32.1: 67.9
	Na2	3.2	12.8	20.1: 79.9
	Na3	1.3	6.7	16.0: 84.0
X = 2.8	Na1	10.7	5.3	67.1: 32.9
	Na2	8.7	7.3	54.7: 45.3
	Na3	2.5	5.5	31.2: 68.8

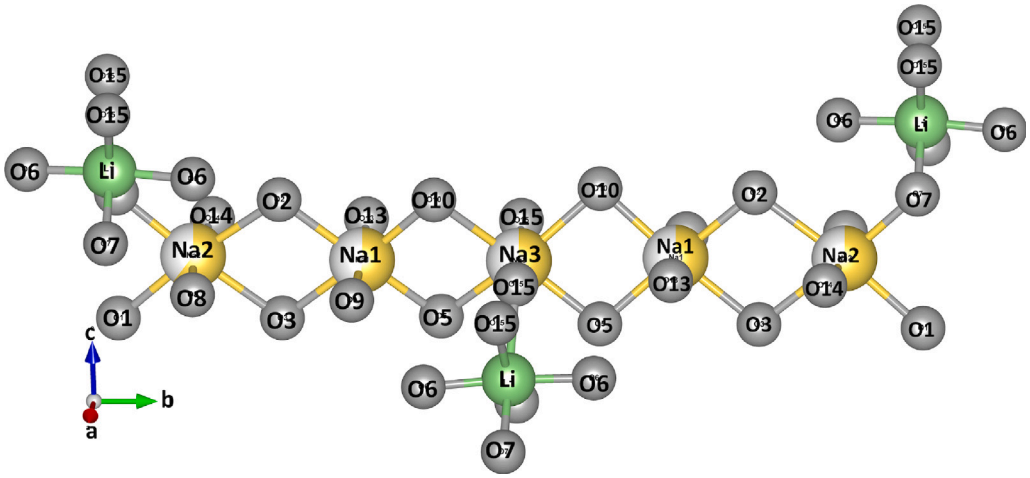

Fig. 5. The bonding scheme in $(Na, Li)O_6$ slabs.

Table 6
Changes of interatomic angles [°] in three compounds of $Li_1(Li_XNa_{5-X})Mo_9O_{30}$.

	X = 0	X = 1.2	X = 2.8
Na2-O3-Na1	101.7(1)	102.6(3)	102.7(3)
Na1-O5-Na3	99.8(1)	99.8(2)	100.3(2)
Na2-O2-Na1	102.2(1)	103.0(1)	103.7(2)
Na1-O10-Na3	94.4(1)	94.6(1)	95.5(2)
Li-O7-Na2	112.9(2)	112.9(2)	113.3(3)
Li-O15-Na3	119.2(3)	119.3(2)	119.5(3)
Mo2-O6-Li	150.5(1)	150.7(1)	151.6(2)
Mo5-O15-Li	95.1(2)	95.1(2)	94.6(3)
Mo1-O7-Li	100.7(1)	100.4(1)	99.8(2)
Mo1-O4-Mo2	100.7(1)	100.4(1)	99.8(2)
Mo4-O12-Mo2	106.0(1)	108.6(1)	105.9(1)
Mo4-O11-Mo5	99.90(1)	99.9(1)	99.7(1)
Mo5-O1-Mo4	106.2(1)	106.0(1)	105.7(1)
Mo4-O11-Mo3	108.48(9)	108.41(9)	108.1(1)
Mo4-O12-Mo2	143.4(1)	143.1(1)	142.9(2)
Mo3-O4-Mo1	145.7(1)	145.5(1)	145.6(2)
Mo3-O4-Mo2	109.4(1)	109.35(9)	109.1(1)
Mo2-O6-Mo1	115.3(1)	115.2(1)	114.7(1)

For X = 0, $Na1O_6$ is distorted only 0.35% with respect to a perfect octahedron (Fig. 4a). Comparably, $Na3O_6$ shows a relatively strong distortion of 1.32%, and $Na2O_6$ does 0.52%. This fashion of site-specific polyhedral distortions holds for X = 1.2 ($Li_1(Li_{1.2}Na_{3.8})Mo_9O_{30}$) and X = 2.8 ($Li_1(Li_{2.8}Na_{2.2})Mo_9O_{30}$), as well.

Compared to Na^+, the smaller cation Li^+ might be away from 6 oxygens in similar distances. Otherwise an irregular coordination [4 short + 2 long] can be formed so that LiO_4 is readily configured, as often observed in Li-bearing compounds [34]. For this reason, the distortion sequence $Na3O_6$ > $Na2O_6$ > $Na1O_6$ can be the main reason for the occupation preference Na1 > Na2 > Na3. However, the Li substitution does not effect local octahedral distortion systematically with increasing X (Fig. 4b).

MoO_6 octahedra are more distorted than LiO_6 and NaO_6. It is common in their distortions with the biggest change in $Li_1(Li_XNa_{5-X})Mo_9O_{30}$ when X = 1.2. This gives rise to −1.449 Debye (= 0.302 e·Å) along the ***c*** axis. The corresponding contribution to the electric polarization for X = 0 and X = 2.8 is smaller with the respective value −1.383 Debye (= −0.288 e·Å) and −1.146 Debye (= −0.239 e·Å) (Tab.A8 in Supplementary).

Nonetheless, the bulk lattice distortions in three main directions differ from each other against the Li substitution X: the lattice extends in ***b*** with increasing X but shrinks in both ***a*** and ***c*** (Table 2). The latter is a matter of expectation for the smaller ionic radius of Li^+ (0.76 Å for 6-fold coordination with O^{2-}) replacing the larger Na^+ (1.02 Å) [35].

Interatomic distances as a function of X gave no explanation for the systematic increase of the lattice parameter $|\boldsymbol{b}|$ (Supplementary Tab.A.5, Tab.A.6, Tab.A.7). The lattice expansion in ***b*** with increasing the Li amount at Na sites can be understood by expansion of the slab of 5er NaO_6 units. This unit is oriented exactly parallel to ***b*** (Fig. 2(b)) and, hence, could be expanded in ***b*** when the angles (∠) of (Na-O-Na) bonds would become larger (Fig. 5). Indeed, ∠(Na2-O2-Na1), ∠(Na2-O3-Na1), ∠(Na1-O5-Na3) and, ∠(Na1-O10-Na3) continuously raise with elevating Li substitution, as listed in Table 6. The other angles in (Li-O-Na)-bonds, i.e., ∠(Li-O7-Na2) and ∠(Li-O15-Na3) enlarged with X contribute to the lattice expansion in ***b***, as well. In contrast, all bonding angles ∠(Mo-O-Mo) within a 9er cluster of MoO_6 (Fig. 1(b)) decrease with increasing X, which can act as an additional contribution to the contraction in both ***a*** and ***c*** directions.

In conclusion, with respect to the lattice without Li substitution for Na (X = 0: $Li_1Na_5Mo_9O_{30}$), chemical stress with X = 1.2 ($Li_1(Li_{1.2}Na_{3.8})Mo_9O_{30}$) and X = 2.8 ($Li_1(Li_{2.8}Na_{2.2})Mo_9O_{30}$) induce the largest lattice deformation along ***a***, showing the respective strain 1.22(3)% and 3.73(4)%. The corresponding strains in ***b*** are −0.01(2)% and −0.08(3)%; those in ***c*** are 0.22(5)% and 0.37(3)%, respectively.

3.3. Chemical compositions resulted from NAA

Within a small uncertainty margin below 4%, NAA data evaluation allowed the determination of quantity of both radioisotopes ^{24}Na and ^{99}Mo, resulting in the atomic ratio of Na/Mo of 0.58(2) and 0.43(2) for Sample#1 and -#2, respectively. These Na/Mo values are pedantic and trustful since Na is as sensitive as Mo when using the NAA

Table 7
The atomic ratios Li/Na (XSD) and Na/Mo (NAA), as well as chemical compositions determined for $Li_1(Li_XNa_{5-X})Mo_9O_{30}$. The chemical formulae from XSD completely accord to those from NAA within experimental uncertainties. *constrained with full occupation (see the main text).

X (XSD)	Li/Na (XSD)	Na/Mo (NAA)	Formula (XSD)	Formula (NAA)
0	0.2*	0.58(2)	$Li_1(Li_0Na_5)Mo_9O_{30}$	$Li_1Na_5Mo_9O_{30}$
1.2	0.58	0.43(2)	$Li_1(Li_{1.2}Na_{3.8})Mo_9O_{30}$	$Li_{2.2}Na_{3.8}Mo_9O_{30}$
2.8	1.73	–	$Li_1(Li_{2.8}Na_{2.2})Mo_9O_{30}$	–

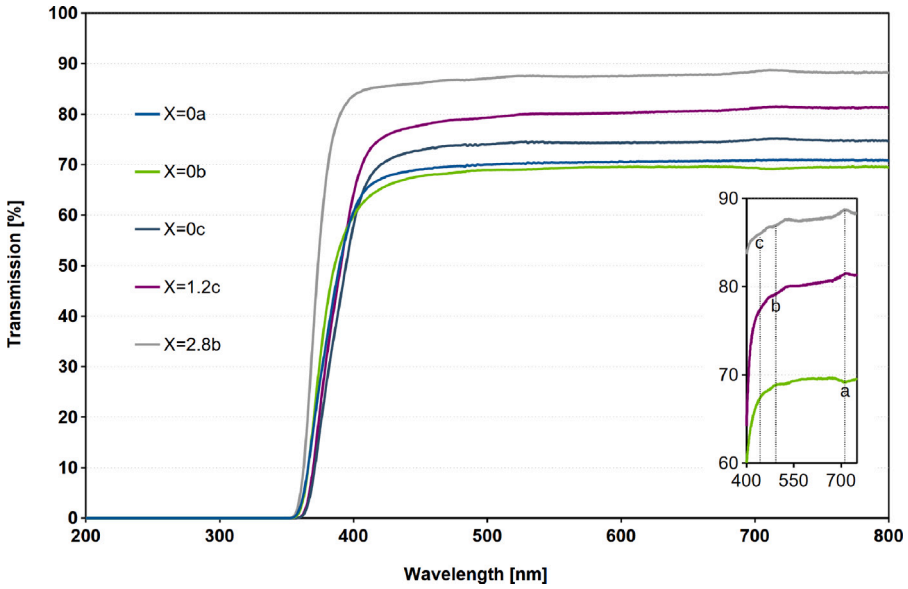

Fig. 6. UV/Vis transmission spectra of $Li_1(Li_XNa_{5-X})Mo_9O_{30}$ with X = 0, 1.2, and 2.8 show both direction- and composition-dependence. Inset shows absorption peaks at 700 nm (a) and 475 nm (b) giving yellowish and green color of crystals, respectively. A weak peak at 455–460 nm (c) for X = 2.8 indicates a portion of the SHG light is absorbed in this Li-rich member.

technique. Hence, even though NAA does not allow element analysis of the light element Li, the amount of Li substitution X could be strictly calculated, i.e., X = 5 - the amount of Na from NAA on the basis of 9 Mo per formula unit. The resulting X = 0 and 1.2 for Sample#1 and -#2 confirmed the chemical formulae $Li_1Na_5Mo_9O_{30}$ and $Li_1(Li_{1.2}Na_{3.8})Mo_9O_{30}$ suggested from XSD data analyses (Table 7). Two solid-solution compounds of $Li_1(Li_XNa_{5-X})Mo_9O_{30}$ with X = 1.2, and 2.8 nearly correspond to a pair of two opposite Li-poor and -rich members, $Li_2Na_4Mo_9O_{30}$ with Li:Na = 2:4 and $Li_4Na_2Mo_9O_{30}$ with Li:Na = 4:2, respectively.

3.4. UV/Vis spectroscopy

A explicit change of the transmission could be seen in UV/Vis spectra of oriented-cut single crystals with varying Li substitution. As shown in Fig. 6, the degree of transmission is strongly dependent on the crystal orientation. For all solid-solution compounds it is commonly valid that the transmission is largest in ***c*** and smallest in ***b*** in the sequence X=0c > X=0a > X=0b. More importantly, UV/Vis spectra could confirm that the transmission is higher with more Li in the structure, e.g., X=2.8b shows about 85% transmission but X=0b does 65% only (Fig. 6).

UV/Vis spectra of the endmember (X = 0) exhibit low transmission with an defined absorption peak near 700 nm (a in the inset in Fig. 6). This dominant red absorption is responsible for greenish tone of Sample#1 (Fig. 3). Further faint absorptions near 475 nm (b in the inset in Fig. 6) are hinted in optical spectra, causing pale yellowish color. Indeed, all our crystals shine with a yellowish-greenish tone in Li-poor members, or pale-yellowish in Li-rich members. It is worth mentioning that a weak absorption near the SHG wavelength of about 455–460 nm (c in the inset in Fig. 6) was adumbrated in UV/Vis spectra of the Li-rich member (X = 2.8). For this absorption the SHG effect is suppressed when X increases from 1.2 for $Li_1(Li_{1.2}Na_{3.8})Mo_9O_{30}$ to 2.8 for $Li_1(Li_{2.8}Na_{2.2})Mo_9O_{30}$. This will be further discussed with the determined NLO coefficients in Section 3.5.

3.5. Optical properties

Refractive indices (n_i) measured with four different wavelengths were used to fit Sellmeier coefficients (Supplementary Table A.9). With these, n_i were calculated for the whole range of 405–650 nm by least-squares. In the conventional definition, n_i (i = 1, 2, 3) are indexed by $n_3 > n_2 > n_1$. In our case, n_1 is in ***b***, n_2 in ***a***, and n_3 in ***c***. n_i increases only insignificantly with increasing X. As an example, n_2 are shown in Fig. 7(a). However, the refractive indices are strongly direction-specific. As shown in Fig. 7(b), the explicit direction-dependence of n_i agrees with previous observations in [11]. A small refractive value corresponds to a high transmission. Hence, the smallest n_3 are in accordance to the largest transmission in ***c*** in Fig. 6.

The SHG light power ($P_{2\omega}$) is related to the refractive index (n_i) of a SHG crystal along the light propagation direction and the incidence angle θ of the incoming fundamental laser, as follows:

$$P_{2\omega}(\theta) = \frac{512\pi^2 d_{ij}^2 P_\omega^2}{c w^2} f(n,\theta)\sin^2\psi = C * f(n,\theta)\sin^2\psi$$

with the incoming beam power P_ω, the beam width w, the speed of light c, and NLO coefficients d_{ij}. i indicates the polarization direction of the SHG beam while j for that of the fundamental beam. $f(n, \theta)$ and $\sin^2\psi$ describe the envelope over the Maker fringe data and the position of the

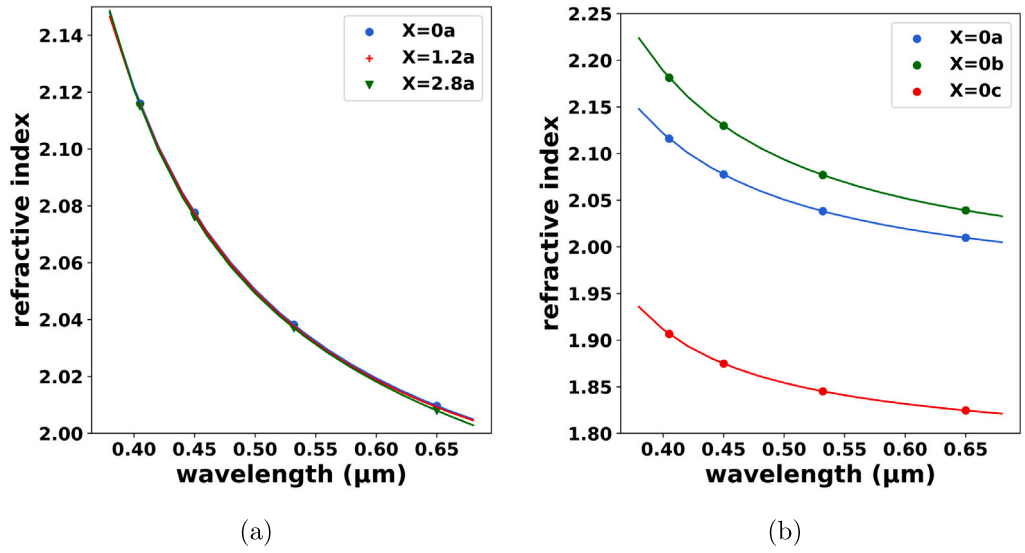

Fig. 7. (a) Refractive indices (n_2) of the ***a*** cuts for all three compositions, showing no significant variations of n_2 with increasing amounts of Li. (b) Refractive indices for X = 0 ($Li_1Na_5Mo_9O_{30}$) are strongly direction-independent (symbols: n_i measured; lines: fitting).

Table 8
Comparison of relative magnitudes of NLO against the Li substitution for Na in $Li_1(Li_XNa_{5-X})Mo_9O_{30}$.

	d_{31} [pm/V]	d_{32} [pm/V]	d_{33} [pm/V]	
X=0	3.6	11	2.9	Literature [11]
X=0	4.2	–	3.4	This study
X=1.2	7.1	18.7	6.2	This study
X=2.8	5.3	15.4	5.1	This study

Table 9
Absolute d_{3j} coefficients from DFT calculations for $Li_1(Li_XNa_{5-X})Mo_9O_{30}$.

	d_{31} [pm/V]	d_{32} [pm/V]	d_{33} [pm/V]
X=0	2.20	2.31	2.16
X=1	2.41	3.28	2.25
X=3	2.36	3.21	2.19

oscillation minima, respectively (more details in [11,31] and literature therein). In a rotational Maker fringe measurement, the rotational axis corresponds to the direction of polarization of the fundamental beam. In our system (SG: ***Fdd*2**), the SHG beam is polarized exclusively parallel to the ***c*** axis for the polar symmetry element 2 [36]. Hence, only relative values of d_{3j} are of interest in this study case.

d_{3j} were evaluated by fitting C from least-square refinements, where d_{3j} and w parameters were refined to fit direction-dependent $P_{2\omega}(\theta)$. The resulting relative NLO coefficients are listed in Table 8. For examples, two different Maker fringes (MFs) data X=0b‖a and X=1.2b‖a resulted in relative values of d_{31}, whereas MFs data X=1.2a‖b delivered d_{32} (Fig. 8). MFs measured in the present study exhibited some asymmetric distribution in shapes over the total intensity. These experimental errors may be attributed to imperfectly polished surfaces of plate samples [12]. And eventual multiple scattering events were not considered [31]. Nonetheless, the relative magnitudes of d_{3j} determined for X = 0 are comparable to those reported by [11] (Table 8), confirming the magnitude order $d_{32} > d_{31} > d_{33}$ for all our samples, as well.

Interestingly, X = 1.2, not X = 2.8, shows the highest magnitude for d_{3j}. When comparing d_{3j}(X = 0) to d_{3j}(X = 2.8), the Li substitution for Na led to the increase of d_{3j} in the solid-solution crystals studied. DFT calculations suggested theoretical absolute magnitudes in the same order d_{3j}(X = 1.2) > d_{3j}(X = 2.8) > d_{3j}(X = 0) (Table 9). Furthermore, a comparison of normalized SHG intensities agrees with the largest SHG beam intensity for X = 1.2, followed by X = 2.8 and X = 0 (Fig. 9). The suppression of SHG in the Li-rich compound (X = 2.8) points to that the SHG beam (455–460 nm) cannot be completely transmitted in the solid-solution crystals when the entire Li/Na ratio is higher than 2/4, despite of increasing transmission with increasing X from 0 to 2.8.

At last, it has to be mentioned that the polarizability (α_{AE}) impacts on linear and non-linear optical behaviors. Using the refined unit cell volumes V_{UC} with n_i measured for 650 nm, α_{AE} for X = 0 ($Li_1Na_5Mo_9O_{30}$), X = 1.2 ($Li_1(Li_{1.2}Na_{3.8})Mo_9O_{30}$), and X = 2.8 ($Li_1(Li_{2.8}Na_{2.2})Mo_9O_{30}$) were calculated using the Anderson-Eggleton relationship [37]:

$$\alpha_{AE} = \frac{(n^2-1)V_{UC}}{4\pi + (4\pi/3 - 2.26)(n^2-1)}$$

The smaller Li^+ polarizes its coordination oxygens more strongly than the larger Na^+, i.e., the more Li within NaO_6, α_{AE} can become larger. However, the resulting averaging α_{AE} are 7.58^{-28} m^3 (X = 0) > 7.47^{-28} m^3 (X = 1.2) > 6.98^{-28} m^3 (X = 2.8). This is not surprising because the negative lattice expansion with increasing X is more dominant than the local octahedral distortion. In addition, Li preferentially occupies the least distorted $Na1O_6$ octahedron, as discussed in Section 3.2. On the other hand, the polarizability in ***b*** = 6.12^{-10} m is much larger than 2.45^{-10} m in ***c*** and 1.19^{-10} m in ***a*** for X = 0. This explains the highest value of d_{32}. Consequently, the SHG effect in the title solid solution might be comprehended in consideration of combining refractive indices, polyhedral distortions, direction-dependent polarizability, the lattice volume and its distortion.

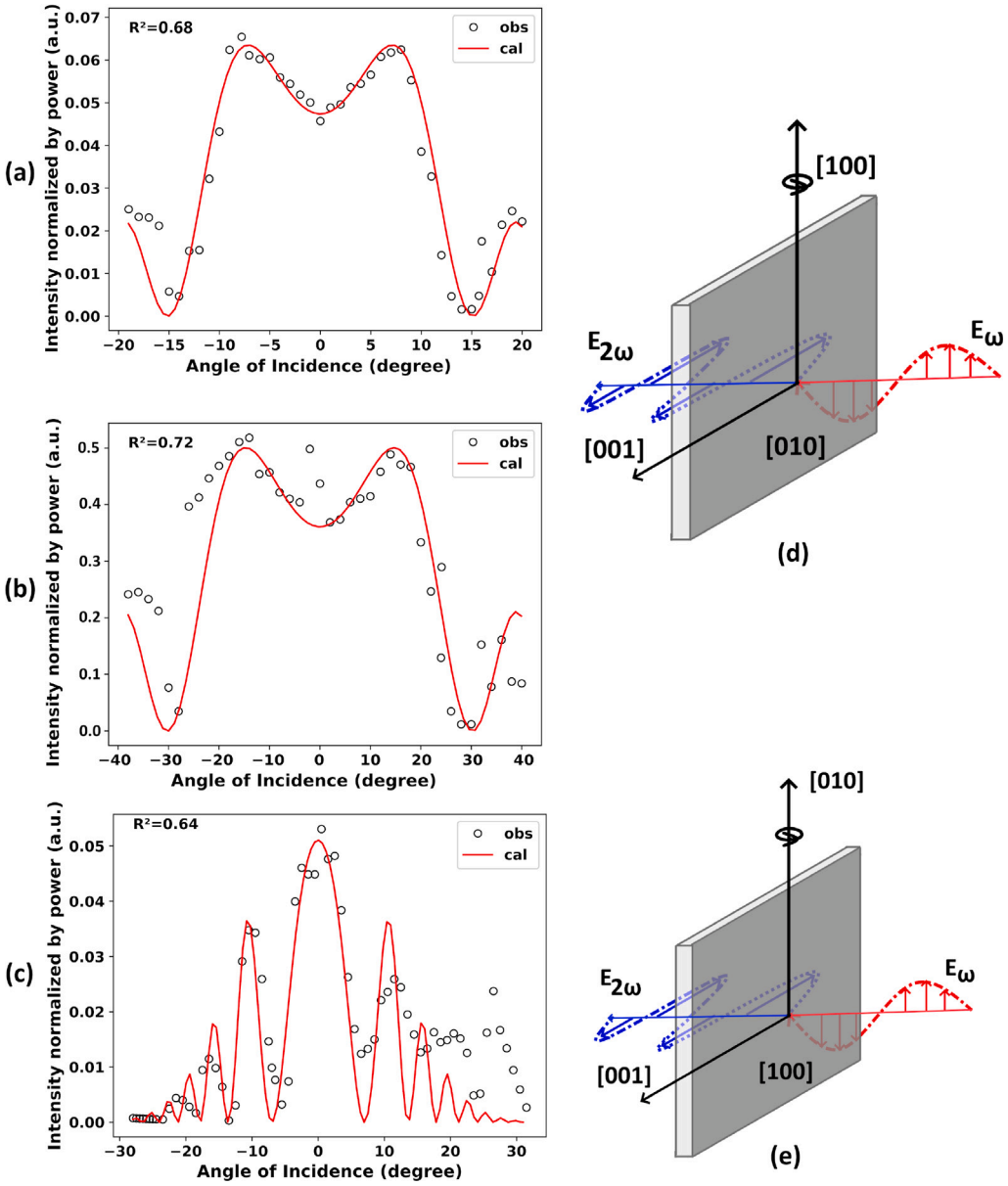

Fig. 8. Observed (circles) and fitted (red lines) MFs in the system $Li_1(Li_XNa_{5-X})Mo_9O_{30}$ for X=0b||a (a) for X=1.2b||a (b) for X=1.2a||b (c). The crystal orientations, the fundamental wave vector E_ω and the SHG wave vector $E_{2\omega}$ were set to determine d_{31} (d) and d_{32} (e).

4. Conclusion

This study applied a combined use of XSD with NAA to deliver accurate structural and compositional contents of three solid-solution compounds $Li_1(Li_XNa_{5-X})Mo_9O_{30}$, X = 0, 1.2 and 2.8, as grown using the Czochralski method. These new compounds crystallize in their common polar space group ***Fdd*2**. Structure refinements using XSD data revealed a preference for the Li substitution within a less distorted octahedron, $Na1O_6$. Overall, max. 56% Na could be replaced by Li.

Direction-dependent transmission and reflective indices were determined to provide their reciprocally proportional values. The crystal of a Li-rich member, $Li_1(Li_{2.8}Na_{2.2})Mo_9O_{30}$ exhibits a high transmission but with weak absorption of the SGH light. This explains the suppressed SHG intensity for X = 2.8 compared to that for X = 1.2. Relative magnitudes and absolute values of d_{3j} agree with d_{3j} for X = 1.2 at largest, as well. So far investigated, $Li_1(Li_{1.2}Na_{3.8})Mo_9O_{30}$ is the best SHG compound among the title solid-solution members, as meeting an optimal compromise for both high transmission by replacing Li for Na and low absorption in the SHG wavelength region.

Comparing the second-order nonlinear coefficients d_{ij} of the known SHG crystals [31], e.g., d_{32} for $LiNbO_3$ = 25.2 pm/V (λ(fundamental) = 1064 nm), d_{32} = 18.7 pm/V (λ(fundamental) = 915 nm) for $Li_1(Li_XNa_{5-X})Mo_9O_{30}$ (X = 1.2) (Table 8) lies in the region of large d_{ij} values of well-known SHG crystals (Table 10 in [31]). Thus, the title solid solution deserves further intensive investigation to industrial application in SHG-based optical devices.

In order to determine defect types and concentrations in the system $Li_1(Li_XNa_{5-X})Mo_9O_{30}$, it is necessary to grow crystals with subtle increments in the critical variable X. At the same time, laser damage threshold experiments might be conducted to deliver concrete effects of the Li substitution on the laser resistance. Such fundamental studies

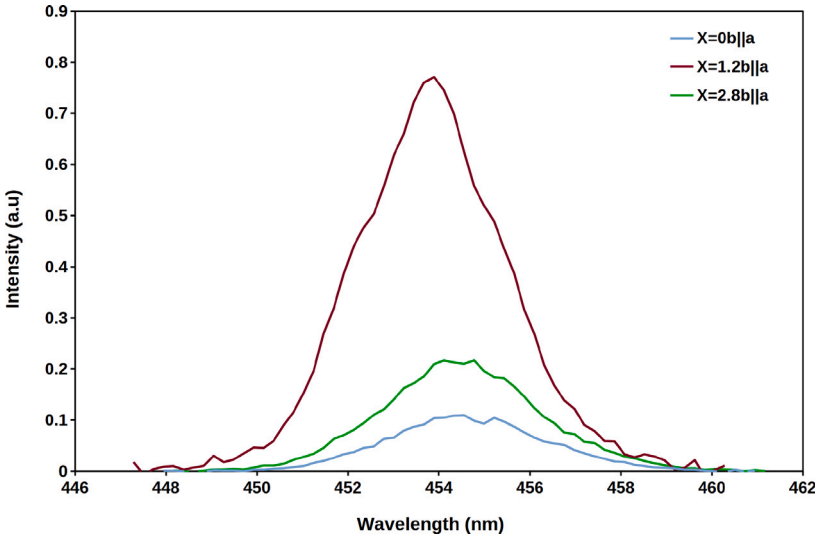

Fig. 9. Comparison of normalized SHG intensity for X = 0 ($Li_1Na_5Mo_9O_{30}$) in pale blue, X = 1.2 ($Li_1(Li_{1.2}Na_{3.8})Mo_9O_{30}$) in red, and X=2.8 ($Li_1(Li_{2.8}Na_{2.2})Mo_9O_{30}$) in green. All three crystals samples were oriented-cut in ***b*** to probe with the fundamental beam polarized in ***a*** at 0° incidence. The SHG intensity of X = 1.2 is significantly higher than those of the other compositions.

of structure-related optical properties could contribute to realize more effective and inexpensive SHG media.

CRediT authorship contribution statement

V.Z. Vuksan: Writing – original draft, Visualization, Investigation, Formal analysis. **Y. Cheng:** Writing – review & editing, Software, Methodology. **S.-H. Park:** Writing – review & editing, Writing – original draft, Validation, Supervision, Methodology, Investigation, Conceptualization. **E.V. Sturm:** Writing – review & editing, Resources. **K. Gméling:** Methodology, Formal analysis. **L. Szentmiklósi:** Writing – review & editing, Methodology.

Declaration of competing interest

The corresponding author SoHyun PARK discloses any potential competing or non-financial interests on behalf of all authors iof the manuscript.

Data availability

Data will be made available on request.

Acknowledgments

SHP thanks Dr. Révay Zsolt at the neutron source Heinz Maier-Leibnitz (FRM II), Garching, Germany for valuable advice for the use of NAA. The NAA measurements were realized as part of the BNC-LENS initiative under the proposal number BNC-LENS-664. Y. Cheng acknowledges Leibniz Supercomputing Centre (LRZ) of the Bavarian Academy of Sciences and Humanities (BAdW), Germany for the provisioning and support of computational resources, as well as the scholarship from China Scholarship Council, China (Project ID#:202204890001). We thankfully acknowledge our colleagues Mariam Kurashvili and Prof. Jochen Feldmann for supporting SHG and MF setups in the Chair for Photonics & Optoelectronics at Department of Physics, LMU, Munich, Germany.

Appendix A. Supplementary data

Supplementary material related to this article can be found online at https://doi.org/10.1016/j.jssc.2024.124920.

References

[1] R.W. Boyd, Chapter 1 - The nonlinear optical susceptibility, in: R.W. Boyd (Ed.), Nonlinear Optics (Third Edition), third ed., Academic Press, Burlington, 2008, pp. 1–67, http://dx.doi.org/10.1016/B978-0-12-369470-6.00001-0.

[2] M. Pinnow, Materials for nonlinear optics: Chemical perspectives, Acta Polymerica 44 (2) (1993) 112, http://dx.doi.org/10.1002/actp.1993.010440216.

[3] M. Schmitt, T. Mayerhöfer, J. Popp, I. Kleppe, K. Weisshart, Light-matter interaction, in: Handbook of Biophotonics, John Wiley & Sons, Ltd, 2013, pp. 87–261, http://dx.doi.org/10.1002/9783527643981.bphot003.

[4] P. Butcher, D. Cotter, The Elements of Nonlinear Optics, in: Cambridge Studies in Modern Optics, Cambridge University Press, 1990.

[5] E. Zharikov, C. Zaldo, F. Díaz, Double tungstate and molybdate crystals for laser and nonlinear optical applications, MRS Bull. 34 (4) (2009) 271–276, http://dx.doi.org/10.1557/mrs2009.78.

[6] B. Binish, B. Lokesh, Y. Veer, S. Peters, M. Abith, T.S. Girisun, K.M. Rahulan, Silver molybdate: An excellent optical limiting material under nanoregime for photonic device application, Sci. Rep. 14 (5642) (2024) http://dx.doi.org/10.1038/s41598-024-53690-0.

[7] D. Spassky, A. Vasil'ev, I. Kamenskikh, V. Kolobanov, V. Mikhailin, A. Savon, L. Ivleva, I. Voronina, L. Berezovskaya, Luminescence investigation of zinc molybdate single crystals, Physica Status Solidi (a) 206 (7) (2009) 1579–1583, http://dx.doi.org/10.1002/pssa.200824311.

[8] T. Bekker, N. Coron, F. Danevich, V. Degoda, A. Giuliani, V. Grigorieva, N. Ivannikova, M. Mancuso, P. de Marcillac, I. Moroz, C. Nones, E. Olivieri, G. Pessina, D. Poda, V. Shlegel, V. Tretyak, M. Velazquez, Aboveground test of an advanced Li2MoO4 scintillating bolometer to search for neutrinoless double beta decay of 100Mo, Astropart. Phys. 72 (2016) 38–45, http://dx.doi.org/10.1016/j.astropartphys.2015.06.002.

[9] A. Annenkov, O. Buzanov, F. Danevich, A. Georgadze, S. Kim, H. Kim, Y. Kim, V. Kobychev, V. Kornoukhov, M. Korzhik, J. Lee, O. Missevitch, V. Mokina, S. Nagorny, A. Nikolaiko, D. Poda, R. Podviyanuk, D. Sedlak, O. Shkulkova, J. So, I. Solsky, V. Tretyak, S. Yurchenko, Development of CaMoO4 crystal scintillators for a double beta decay experiment with Mo100, Nucl. Instrum. Methods Phys. Res. A 584 (2) (2008) 334–345, http://dx.doi.org/10.1016/j.nima.2007.10.038.

[10] Y.S. Sistla, R.G. Burela, A. Gupta, N. Tabassum, Optical, thermal, and mechanical properties of scheelite molybdate and tungstate materials using atomistic simulations, in: R.K. Tyagi, P. Gupta, P. Das, R. Prakash (Eds.), Advances in Engineering Materials, Springer Nature Singapore, Singapore, 2024, pp. 169–183.

[11] W. Zhang, H. Yu, J. Cantwell, H. Wu, K. Poeppelmeier, S. Halasyamani, LiNa5Mo9O30: Crystal growth, linear and nonlinear optical properties, Chem. Mater. 28 (2016) http://dx.doi.org/10.1021/acs.chemmater.6b01756.

[12] J. Jerphagnon, S.K. Kurtz, Maker fringes: A detailed comparison of theory and experiment for isotropic and uniaxial crystals, J. Appl. Phys. 41 (4) (1970) 1667–1681, http://dx.doi.org/10.1063/1.1659090.

[13] V. Sukharev, A. Sadovskiy, E. Sukhanova, A. Dovnarovich, D. Spassky, K. Podurec, A. Kaloyan, V. Nagirnyi, S. Omelkov, I. Avetissov, Crystal growth and luminescent properties of $LiNa_5Mo_9O_{30}$, J. Cryst. Growth 519 (2019) 35–40, http://dx.doi.org/10.1016/j.jcrysgro.2019.05.008.

[14] H. Hamza, I. Ennajeh, M.F. Zid, A. Driss, $LiNa_5Mo_9O_{30}$, Acta Crystallogr. E 68 (11) (2012) i80–i81, http://dx.doi.org/10.1107/S1600536812041876.

[15] U. Gattermann, B. Röska, C. Paulmann, S.-H. Park, Large single crystal growth of $MnWO_4$-type materials from high-temperature solutions, J. Cryst. Growth 453 (2016) 40–48, http://dx.doi.org/10.1016/j.jcrysgro.2016.07.039.
[16] Agilent, SCALE3 ABSPACK – an agilent technologies program (1.0.11, gui: 1.0.7), Agilent Technologies Ltd, Yarnton, Oxfordshire, England, 2005-2012.
[17] Agilent, CrysAlis PRO, Agilent Technologies Ltd, Yarnton, Oxfordshire, England, 2014.
[18] G.M. Sheldrick, A short history of SHELX, Acta Crystallogr. A 64 (1) (2008) 112–122.
[19] V. Petříček, L. Palatinus, J. Plášil, M. Dušek, Jana2020 – A new version of the crystallographic computing system jana, Z. Kristallogr. - Crystall. Mater. 238 (7–8) (2023) 271–282, http://dx.doi.org/10.1515/zkri-2023-0005.
[20] K. Momma, F. Izumi, *VESTA*: A three-dimensional visualization system for electronic and structural analysis, J. Appl. Crystallogr. 41 (2008) 653–658, http://dx.doi.org/10.1107/S0021889808012016.
[21] Z. Song, Z. Li, J. Zhang, Z. Chen, L. Suescun, Q. Liu, BFIP: an online tool to calculate the best fitted idealized polyhedron, J. Appl. Crystallogr. 56 (3) (2023) 884–888, http://dx.doi.org/10.1107/S160057672300328X.
[22] I.D. Brown, D. Altermatt, Bond-valence parameters obtained from a systematic analysis of the Inorganic Crystal Structure Database, Acta Crystallogr. AB 41 (4) (1985) 244–247, http://dx.doi.org/10.1107/S0108768185002063.
[23] L. Szentmiklósi, D. Párkányi, I. Sziklai-László, Upgrade of the Budapest neutron activation analysis laboratory, J. Radioanal. Nucl. Chem. 309 (2016) 91–99, http://dx.doi.org/10.1007/s10967-016-4776-7.
[24] D. Bagayoko, Understanding Density Functional Theory (DFT) and completing it in practice, AIP Adv. 4 (12) (2014).
[25] Y. Cheng, R. He, Y. Xia, T. Han, L. Fang, S. Huang, B. Liu, Sound velocities, and mechanical and electronic properties of the intermetallic compound $CeAl_2$ at high pressure, Phys. Rev. B 105 (6) (2022) 064106.
[26] G. Guo, K. Chu, D.-s. Wang, C.-g. Duan, Linear and nonlinear optical properties of carbon nanotubes from first-principles calculations, Phys. Rev. B 69 (20) (2004) 205416.
[27] P.D. Borges, L.M. Scolfaro, H.W. Leite Alves, E.F. da Silva, DFT study of the electronic, vibrational, and optical properties of SnO2, Theoret. Chem. Accounts 126 (2010) 39–44.
[28] S.J. Clark, M.D. Segall, C.J. Pickard, P.J. Hasnip, M.I. Probert, K. Refson, M.C. Payne, First principles methods using CASTEP, Z. Kristallogr.-Crystall. Mater. 220 (5–6) (2005) 567–570.
[29] K. Lejaeghere, V. Van Speybroeck, G. Van Oost, S. Cottenier, Error estimates for solid-state density-functional theory predictions: an overview by means of the ground-state elemental crystals, Crit. Rev. Solid State Mater. Sci. 39 (1) (2014) 1–24.
[30] J.P. Perdew, K. Burke, M. Ernzerhof, Generalized gradient approximation made simple, Phys. Rev. Lett. 77 (18) (1996) 3865.
[31] I. Shoji, T. Kondo, A. Kitamoto, M. Shirane, R. Ito, Absolute scale of second-order nonlinear-optical coefficients, J. Opt. Soc. Am. B 14 (9) (1997) 2268–2294, http://dx.doi.org/10.1364/JOSAB.14.002268, URL https://opg.optica.org/josab/abstract.cfm?URI=josab-14-9-2268.
[32] D. Brewster, IX. On the laws which regulate the polarisation of light by reflexion from transparent bodies, Philos. Trans. R. Soc. Lond. 105 (1815) 125–159, http://dx.doi.org/10.1098/rstl.1815.0010.
[33] M. Born, E. Wolf, Principles of Optics: 60th Anniversary Edition, Seventh ed., Cambridge University Press, 2019.
[34] F. Liebau, Structural Chemistry of Silicates: Structure, Bonding, and Classification, Springer-Verlag, 1985, URL https://books.google.de/books?id=AwfwAAAAMAAJ.
[35] R.D. Shannon, Revised effective ionic radii and systematic studies of interatomic distances in halides and chalcogenides, Acta Crystallogr. A 32 (5) (1976) 751–767, http://dx.doi.org/10.1107/S0567739476001551, URL https://onlinelibrary.wiley.com/doi/abs/10.1107/S0567739476001551.
[36] D.A. Kleinman, Theory of second harmonic generation of light, Phys. Rev. 128 (1962) 1761–1775, http://dx.doi.org/10.1103/PhysRev.128.1761, URL https://link.aps.org/doi/10.1103/PhysRev.128.1761.
[37] R.D. Shannon, R.X. Fischer, Empirical electronic polarizabilities of ions for the prediction and interpretation of refractive indices: Oxides and oxysalts, Am. Mineral. 101 (10) (2016) 2288–2300, http://dx.doi.org/10.2138/am-2016-5730.